Acta Materialia 211 (2021) 116885

Quantitative prediction of rapid solidification by integrated atomistic and phase-field modeling

Sepideh Kavousi[1], Brian R. Novak[2], Dorel Moldovan[2,3], and Mohsen Asle Zaeem[1]*

[1] Department of Mechanical Engineering, Colorado School of Mines, Golden, CO 80401, USA
[2] Department of Mechanical and Industrial Engineering, Louisiana State University, Baton Rouge, LA 70803, USA
[3] Center for Computation and Technology, Louisiana State University, Baton Rouge, LA 70803, USA

Abstract

Systematic integration of atomistic simulations with phase-field modeling is presented for quantitative predictions of cellular growth and solute trapping during solidification of alloys for solidification velocities relevant to additive manufacturing. For parametrization of the phase-field model, molecular dynamics simulations are utilized as an alternative to complex experiments to obtain the anisotropic crystal-melt interface free energy, kinetic coefficient, and diffusive interface velocity. The accuracy of this integrated model is tested for rapid solidification of Ti-3.4at.%Ni alloy. The predicted solute trapping of the proposed phase-field model is comparable with the continuous growth model for solidification velocities of additive manufacturing. The predicted primary dendritic arm spacing is weakly dependent on the diffuse interface width enabling simulations in larger length scales. The concentration profile and partition coefficient obtained from both two-and three-dimensional phase-field simulations are comparable to the results of Kurz-Fisher's analytical and continuous growth models, respectively. Unlike other computational models for rapid solidification, the proposed model enables predictions completely based on computations without any fittings to experiments.

Keywords: Rapid Solidification; Phase-field modeling; Molecular dynamics; Solute trapping; Cellular growth.

*Corresponding author: zaeem@mines.edu (M. Asle Zaeem)

1 Introduction

Additive manufacturing (AM) is an innovative and novel technique where the final three-dimensional parts are fabricated by the layer-upon-layer joining of the material [1]. This method is used for producing complex parts with small material waste and reduced manufacturing time, which makes it a unique and popular technique. Although AM is a growing manufacturing technique that has the potential to phase out multiple traditional manufacturing methods [2], it is accompanied by numerous technical challenges regarding the design, materials, and process modeling and control [3].

AM of metallic alloys is a rapid solidification process, characterized by cooling rates as large as 10^4- 10^6 K/s [4-7]. Increasing solidification velocity reduces the partitioning and stretches the solute solubility limit, which in turn affects the mechanical properties [1, 8-10]. Besides, the directionality of heat extraction during the AM can lead to the formation of columnar grains. They all result in anisotropy and heterogeneity in microstructures and mechanical properties [11, 12], which all are functions of processing parameters [12].

Development of accurate modeling and simulation techniques reduces the need for experimental tests aimed at prediction and control of the quality and material properties of the final products [1, 13]. The ultimate goal of modeling and simulations of AM processes is to obtain reliable processing-structure relations comparable with reality [2], and this requires a deep insight into the relationship between the microstructure, processing parameters, and properties of the final products. There are different numerical models to simulate the microstructure evolution during the solidification, such as the phase-field (PF) [14-16], cellular automata [17-19], Monte Carlo (MC) [20, 21], and dendritic needle network methods [22, 23]. Among these, the PF method is a well-established approach used to investigate the microstructure evolution during solidification, which utilizes a diffuse solid-liquid interface width to overcome some of the limitations of other models [14, 24-29].

Accurate predictions of segregation and dendritic structures often require very high computational costs. This problem is even more critical in PF models for rapid solidification that exhibit a dependency on the diffuse interface width. The pioneer PF models, such as the Echebaria-Folch-Karma-Palpp (EFKP) model [14], considered no chemical potential jump across the interface, which is only valid when the CM interface is in local equilibrium. The EFKP model can provide accurate prediction of stability spectrum of a planar steady-state interface by using interface width twenty times the capillary length and for solidification velocities smaller than 100 μm/s [14]. However, this model fails to predict accurate solute trapping behavior during rapid solidification unless the interface width is in the order of capillary length [27, 30]. Some other PF studies used the model developed by Pinomaa and Provatas [31] to compare the segregation and primary dendritic arm spacing (PDAS) results with the experimental data and analytical models [29, 32, 33]. However, accuracy results were obtained only for the cases where the diffuse interface width is in the order of the smallest physically relevant length-scale in the solidification problem, which is the capillary length [29, 32]. To overcome this problem, Kavousi and Asle Zaeem [32] have recently developed a quantitative PF model that can accurately predict the micro-segregation for a broader range of solidification velocities, and the model dependency on the interface width is insignificant. The thin interface analysis of this model relates the PF model parameters to material properties, such as the crystal-melt (CM) interface free energy, kinetic coefficient, and diffusive interface velocity [32]. The diffusive interface velocity was calculated experimentally for a very limited group of binary systems [34, 35]. Different experimental techniques such as grain boundary groove [36-38] and homogeneous nucleation [39] were implemented to calculate the CM interface free energy. Meanwhile, there are very few studies on measurements of the anisotropic CM interface energy [40]. The kinetic coefficient for solidification can be obtained from the experimental velocity-undercooling relationship [41, 42]. But to the best of our knowledge, there is no experimental study to determine the orientation-dependent kinetic coefficient. Due to the limitations of the experimental techniques, and their complexity and cost, reliable computational simulations may be used to calculate high-temperature material properties for quantitative solidification models.

Aziz et al. [43] proposed an analytical model, known as the continuous growth (CG) model, that predicts the non-equilibrium partition coefficient by comparing the solidification velocity to the diffusive velocity. This model predicts that the partition coefficient increases asymptotically, and complete solute trapping occurs when the solidification velocity goes to infinity. The diffusive velocity (or the diffusive interface velocity) in the CG model is the speed of solute-solvent redistribution at an infinite driving force [44]. Diffusive velocity can be obtained by fitting the solidification velocity versus partition coefficient data obtained from either experiments [45] or MD simulations [46-48] to the CG model.

MD simulations based on the capillary fluctuation method were used to calculate the CM interface free energy and corresponding anisotropy strength for metals [49-51], and binary [52-54] and ternary [55] alloys. Besides, the kinetic coefficient for the solidification of metals was estimated for different metallic elements [49, 51, 56] based on the method introduced by Hoyt et al. [57]. Recently, Kavousi et al. [48] proposed an atomistic approach, based on MD and MC simulations, to calculate the kinetic coefficient of a binary system based on the CG model.

In this paper, we introduce a computational framework by integrating atomistic and PF modeling to study rapid solidification of metallic alloys. We test this framework for solidification of Ti-3.4 at.% Ni. In this process, we utilize our recently developed interatomic potential for Ti-Ni alloys [52], which is capable of predicting high-temperature thermo-physical properties and solidification partitioning behavior similar to the experimental and first-principles data. Ti and its alloys, depending on the alloying elements, are classified into three main groups as α-type (with hcp crystal structure), β-type (with bcc structure), and α+ β- type [58]. The addition of other alloying elements such as V, Mo, Ta, or Cr stabilizes the β phase while adding elements such as Ni, Fe, Cu, or B stabilizes the α-phase [58]. Although heat treatments can change the mechanical properties of most alloy parts via altering the microstructure [2], one important fact about Ti alloys is that some of their properties do not change considerably during heat treatment. For instance, heat treatment of Ti-6Al-4 V affects the distribution, size, and morphology of α-grains but it does not have a noticeable effect on the prior beta grains, which control some important properties such as the fatigue response [59]. On the other hand, creating the desired microstructures by AM without requiring any subsequent heat treatments can significantly reduce the cost and time of part fabrication. Thus, it is important to predict and control the as-built microstructures of the AM alloys.

The proposed computational framework enables quantitative predictions of solute trapping and cellular growth behavior during rapid solidification without requiring complex melting and solidification experiments or fitting to experimental data. We show how the PF equations are parametrized with the material properties, including the CM interfacial free energy, kinetic coefficient, and diffusive velocity, calculated from specifically designed MD simulations. To demonstrate the accuracy of this computational framework, its solute trapping predictions are benchmarked against the partition coefficient obtained from MD simulations and the concentration profiles from analytical models. In addition, we investigate and report on how solute trapping affects cellular growth by calculating the primary dendritic arm spacing.

2 Simulation Methodology

In this section, we present the fundamentals of the PF model followed by the descriptions of MD simulations required to parametrize the PF model.

2.1 Phase-field modeling of solidification

We present the main equations of the PF model developed recently by Kavousi and Asle Zaeem [32] for accurate prediction of the solute trapping behavior during rapid solidification. The order parameter (ϕ) and concentration (c) fields are used to describe the microstructure evolution during the solidification. The order parameter is defined as a continuous function that distinguishes between the solid and liquid phases. The PF model has the benefit of not tracking the interface explicitly unlike the front tracking models [60]. However, the diffuse description of the interface introduces some non-equilibrium effects into the PF equations which requires modifications based on the physics of solidification. The evolution equations for order parameter and dimensionless supersaturation (U) during solidification of a binary alloy are given by [32]:

$$\tau(\boldsymbol{n})\frac{\partial\phi}{\partial t}=\left[\nabla.\left[W(\boldsymbol{n})^2\,\boldsymbol{\nabla}\phi\right]+\sum_{i=1}^{2}\partial_i\left[W(\boldsymbol{n})\frac{\partial W(\boldsymbol{n})}{\partial(\partial_i\phi)}\,|\boldsymbol{\nabla}\phi|^2\right]\right]+\phi^3-\phi-\frac{\lambda}{1-\mathrm{k_e}}(1-\phi^2)^2\left(exp(u)-1+\frac{G(y-Vt)}{\frac{\mathrm{m_L^e c_0^L}}{\mathrm{k_e}}}\right), \tag{1}$$

$$\left(\frac{1+k_e}{2}-\frac{1-k_e}{2}\phi\right)\frac{\partial U}{\partial t}=\boldsymbol{\nabla}.\left(D_L\frac{1-\phi}{2}\boldsymbol{\nabla}U\;+\boldsymbol{j_{at}}\right)+\left[1+(1-k_e)U\right]\frac{1}{2}\frac{\partial\phi}{\partial t}, \tag{2}$$

$$\boldsymbol{j_{at}}=a_t(\phi)W_\phi\left[1+(1-\mathrm{k_e})U\right]\frac{\partial\phi}{\partial t}\frac{\boldsymbol{\nabla}\phi}{|\boldsymbol{\nabla}\phi|}. \tag{3}$$

For an alloy with the composition $\mathrm{c_0^L}$, the equilibrium partition coefficient $\mathrm{k_e}$ and liquidus line slope $\mathrm{m_L^e}$ can be obtained from the phase diagram. $W(\boldsymbol{n})$ and $\tau(\boldsymbol{n})$, with magnitudes of W_ϕ and τ_ϕ, are the anisotropic interface width and the characteristic time, respectively, which are functions of the unit vector normal to the interface and pointing into the liquid, $\boldsymbol{n}$. λ is a parameter related to the magnitude of capillary length, d_0, as given by Equation (8). u is the dimensionless chemical potential, which is related to c and U as:

$$u = \ln\left(\frac{2c\mathrm{k_e}/\mathrm{c}_0^{\mathrm{L}}}{1+\mathrm{k_e}-(1-\mathrm{k_e})\phi}\right), \tag{4}$$

$$U = \frac{e^{u}-1}{1-\mathrm{k_e}}\,. \tag{5}$$

For simulating the directional solidification, the change of temperature field, T, along the growth direction y is described as $T(y,t) = T_0 + G(y - Vt)$, where T_0 is a reference temperature, V is the pulling velocity (the interface velocity in directional solidification), and G is the thermal gradient. The anti-trapping flux in this model is given by [32]:

$$a_t(\phi\,) = \frac{1}{2\sqrt{2}}\left(1 - \frac{\mathrm{c}_2}{\ln(1+\varepsilon)}(1-\phi^2)\right), \tag{6}$$

where c_2 controls the amount of solute trapping and $\varepsilon = W_\phi/\mathrm{d}_0$:

$$\mathrm{c}_2 = \frac{1}{4(1\text{-}\mathrm{k_e})}\frac{\mathrm{V_s}}{\mathrm{V_D^{CG}}}\ln\left(\frac{\mathrm{k_e}+1}{2\mathrm{k_e}}\right). \tag{7}$$

$\mathrm{V_s}$ is the ratio of liquid diffusivity, $\mathrm{D_L}$, to $\mathrm{d_0}$, and $\mathrm{V_D^{CG}}$ is the diffusive velocity in the CG model. The parameter c_2, as well as the chemical potential jump (shown by the thin interface analysis), are independent of W_ϕ; therefore, the change in interface width does not affect the solute trapping noticeably.

As a result of the thin interface asymptotic analysis, the relation between the anisotropic capillary length $\mathrm{d}(\vec{n})$ and the kinetic coefficient $\beta(\vec{n})$ with the PF parameters are given as [32]:

$$\mathrm{d}(\vec{n}) = \mathrm{a}_1\frac{W(\vec{n})}{\lambda}, \tag{8}$$

$$\beta^{+}(\vec{n}) = \frac{\mathrm{a}_1\tau(\vec{n})}{\lambda W(\vec{n})}\frac{\mathrm{J}}{A}\left(\frac{k}{\mathrm{k_e}}\right)^{-\frac{1}{4}} - (1+(1\text{-}\mathrm{k_e})U_0^{in})\frac{W(\vec{n})}{D_L}\frac{\mathrm{J}F+K}{2\mathrm{J}}, \tag{9}$$

$$\beta^{-}(\vec{n}) = \frac{\mathrm{a}_1\tau(\vec{n})}{\lambda W(\vec{n})}\frac{\mathrm{J}}{A}\left(\frac{k}{\mathrm{k_e}}\right)^{\frac{3}{4}} - (1+(1\text{-}\mathrm{k_e})U_0^{in})\frac{W(\vec{n})}{D_L}\frac{\mathrm{J}F+K}{2\mathrm{J}}. \tag{10}$$

The + (–) represents if the kinetic coefficient is obtained based on the value from the liquid (solid) side of the interface corresponding to zero (full) solute drag. In Equations (8)-(10), $\mathrm{a}_1=5\sqrt{2}/8$, and J, A, F, and K are defined by Equations (11)-(15) which can be obtained numerically by setting $\phi_0^{in} = -\tanh(\eta/\sqrt{2})$.

$$\mathrm{J} = \int_{-1}^{1} \left(1-\phi_0^{in^2}\right)^2 d\phi_0^{in}, \tag{11}$$

$$A = \int_{-1}^{1} \left(\frac{k}{\mathrm{k_e}}\right)^{\frac{\phi_0^{in^2}}{4}+\frac{\phi_0^{in}}{2}} \left(1-\phi_0^{in^2}\right)^2 d\phi_0^{in}, \tag{12}$$

$$p\left(\phi_0^{in}\right) = \frac{\left(h(\phi_0^{in})-1\right)-2\mathrm{c}_1\partial_\eta\phi_0^{in}}{q\left(\phi_0^{in}\right)}, \tag{13}$$

$$K = \int_{-\infty}^{\infty} \left(1-\phi_0^{in^2}\right)^2 \partial_\eta\phi_0^{in} \left(\int_0^{\eta} p\left(\phi_0^{in}\right) d\xi\right) d\eta, \tag{14}$$

$$F = F^{\pm} = \int_0^{\pm\infty} \left\{ p\left(\phi_0^{in}(\xi)\right) - p\left(\phi_0^{in}(\pm\infty)\right)\right\} d\xi . \tag{15}$$

k is the nonequilibrium partition coefficient, and in the CG model, it can be written in terms of the interface velocity, V [61]:

$$k^{CG}(V) = (\mathrm{k_e} + V/\mathrm{V_D^{CG}})/(1 + V/\mathrm{V_D^{CG}}) \tag{16}$$

$\mathrm{V_D^{CG}}$ is the ratio of interface diffusivity to the interface width which cannot be calculated directly [62]; Thus, it is estimated by fitting the velocity-dependent partition coefficient from specialized experiments or MD simulations to the CG model (Equation(16)).

The anisotropic material properties and non-equilibrium partition coefficients are required to perform quantitative PF simulations. MD simulations are used to obtain the material properties, such as $\beta(\vec{n})$, $\mathrm{d}(\vec{n})$, $\mathrm{V_D^{CG}}$, $\mathrm{D_L}$, and γ(CM interface free energy), that will be used to determine the PF model parameters through the thin interface analysis. In the following section, details of the MD simulations used for parameterizing the PF model are provided.

2.2 Molecular dynamics simulations

We utilize MD simulations for calculating the equilibrium partition coefficient, freezing range, diffusion coefficient, anisotropic CM interface free energy, kinetic coefficient, and the interface diffusive velocity. The solute concentration in each phase will affect all the material properties which are all calculated by MD simulations.

We first calculate the phase diagram before determining the required properties by MD simulations. We use our recently developed modified embedded-atom method (MEAM) interatomic potential for the Ti-Ni binary systems which accurately predicts the high-temperature thermophysical and kinetic properties [52], making it suitable for this study. The MD simulations are performed using LAMMPS (Large-scale Atomic/Molecular Massively Parallel Simulator) [63]. The post-processing of MD simulations is carried out using python packages and libraries such as MDTraj [64] and lmfit [65]. We used Ovito [66] for visualizing the trajectory files.

2.2.1 Phase diagram

The coexistence method with hybrid MC and MD simulations is employed to calculate the phase diagram. For each temperature, the simulation starts from the coexistence of solid and liquid with an approximate concentration equal to the corresponding value from the experimental phase diagram. Then the simulation system is equilibrated in the NPT ensemble for at least 3ns. Every 5000 steps during the equilibration process, we perform 1000 MC swap attempts for atoms of different types. The simulation continues until the solute concentration in both solid and liquid phases does not change for at least 500 ps. The calculated concentrations of solid and liquid phases are used as the initial concentrations in the second round of the coexistence simulations. This loop continues until the error drops below 3%. Additional details regarding the calculations of Ti-rich portion of Ti-Ni binary system and the comparison of the MD-calculated phase diagram with the one from Thermo-Calc are presented in our previous works [52]. For the alloy composition of interest, Ti-3.4 at.% Ni, the temperature for the target liquidus composition, and corresponding partition coefficient are 1860 K and 0.26, respectively.

2.2.2 Crystal-melt interface free energy

The capillary fluctuation method is a well-established method for calculating the CM interface free energy (γ) [49, 67]. In this method, the stiffness of the interface is related to the amplitude of its fluctuations in a fully-equilibrated system. Thus, interface free energy calculations require an accurate determination of the interface position and its evolution over time. The simulation system, presented in Figure 1(a), is a quasi-two-dimensional simulation system with one dimension (y-direction) much smaller than the other dimensions, and the CM interface normal is parallel to the z-direction. The deviation of the interface position, $h(x)$, from its average value, $\langle h \rangle$, is written as a summation of Fourier modes. Accordingly, the interface stiffness, $\gamma + d^2\gamma/d\theta^2$, is linked to the Fourier amplitudes, $A(k)$, and mode numbers, k [49]:

$$h(x) - \langle h \rangle = \sum_k A(k)\, e^{ikx} \,, \tag{17}$$

$$\gamma + d^2\gamma/d\,\theta^2 = \frac{\mathrm{k_B}T}{\mathrm{bW}\langle|A(k)|^2\rangle k^2}. \tag{18}$$

$\mathrm{k_B}T$ is the thermal energy, bW is the cross-sectional area of the interface, and θ is the angle between the local interface normal and the z-direction. For interface energy calculations, it is important to have the simulation system at equilibrium to only obtain the CM interface fluctuations without its net movements due to the solid-liquid phase transformation. The equilibrium compositions in the solid and liquid phases and the corresponding temperature for the simulation are chosen based on the MD-calculated phase diagram. The simulation system is initialized on a lattice with 80×4×120 bcc unit-cells. The central part of the simulation system is melted under the isothermal-isochoric ensemble (NVT) such that the average CM interface normal is parallel to the z-direction. Then the concentrations in the solid and liquid phases are set to the solidus and liquidus concentrations at the target temperature, and the whole system is equilibrated for 1ns in the isothermal-isobaric ensemble ($\mathrm{NP_{zz}T}$), with the barostat applied only to the normal stress along the z-direction which is set to zero. Subsequently, MD simulation under the isothermal-isobaric ensemble (NPH) ensemble is performed for 240 ps, and every 1 ps the configuration of atoms is saved for further analysis of interface fluctuations. The CM interface free energy is an anisotropic property, and the simulations are repeated using different crystallographic orientations along the interface normal direction.

Next, we need to accurately define the interface position and its fluctuations as a function of time. The interface position is obtained through an order parameter, ψ, constructed based on comparing the positioning of each atom's neighbors with the corresponding neighbors in the perfect crystal. ψ is expected to have a lower value in the solid phase compared to the liquid, but as the working temperatures are high, ψ has large fluctuations making the interface determination more difficult. Thus, another order parameter is determined which uses a smoothing function to smooth the values of ψ over a cylindrical region centered on the atoms [50]. The size of the simulation system in the y-direction is small. Therefore, for the interface energy calculations, we consider the CM interface to be semi-one-dimensional with no curvature along the y-direction.

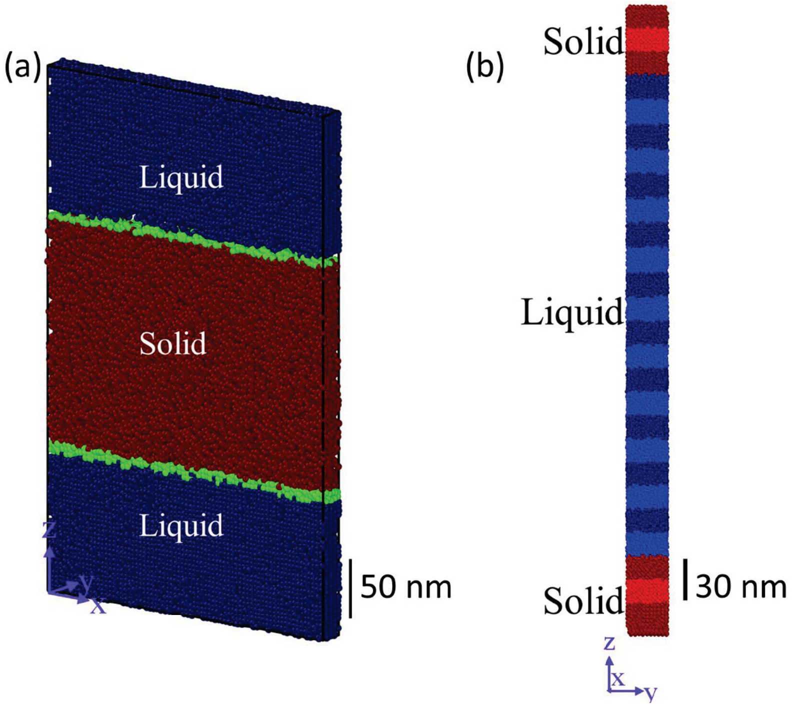

Figure 1. a) A snapshot of the MD simulation for calculation of the CM interface free energy, and b) Initial configuration of the free solidification simulations. The red, blue, and green colors represent the atoms located in solid phase, liquid phase, and solid-liquid interface, respectively. The shades denote the regions thermostatted independently.

2.2.3 Kinetic coefficient

The kinetic coefficient determines how fast the simulation system responds to different solidification driving forces. The driving force for solidification can be generated by reducing the temperature of the simulation system below the equilibrium temperature or by reducing the concentration of solute in the bulk liquid phase below the equilibrium liquidus value ($\mathrm{c}_0^{\mathrm{L}}$). In this study, we promoted solidification by reducing the concentration of solute. The logic behind the method selection is discussed in section 3.2. The relationship between the kinetic coefficient (β) and V is given by Equations (19) and (20) [61].

$$\beta = \frac{1-\frac{c_L}{\mathrm{c}_0^{\mathrm{L}}}\times f(k)}{(1-k)V}, \tag{19}$$

$$f\big(k(V)\big) = \frac{[k+(1-k)\mathfrak{D}]\log\left(\frac{k}{\mathrm{k_e}}\right)+1-k}{1-\mathrm{k_e}}. \tag{20}$$

In these equations, c_L is the steady-state concentration on the liquid side of the interface, which is different from the initial concentration of the bulk liquid phase, and additional analyses of the trajectory files are needed to calculate c_L. The drag coefficient, $\mathfrak{D}$, is a parameter estimating the portion of the overall free energy change during solidification due to the solute diffusion, and the remaining effective free energy is available for solidification. The drag coefficient is determined such that it gives the best linear relationship between the effective free energy and the interface velocity [48, 68]. The free energies are computed using thermodynamic integration and semi-grand canonical ensemble simulations. More detailed information on the methodology for determining the kinetic coefficient can be found in work by Kavousi et al. [48].

2.2.4 Diffusive interface velocity

MD simulations can be used to obtain the non-equilibrium partition coefficients for estimating $\mathrm{V_D^{CG}}$ [48, 68]. The initial simulation system consists of CM coexistence, as presented in Figure 1(b), where the composition of solid and liquid phases are set to the solidus and liquidus values at the target temperature of T=1860 K. First, a solid phase with 10×10×160 bcc unit-cells and the composition of Ti-0.9 at.% Ni is generated. Then the system is equilibrated in the NPT ensemble for 300 ps. The central part of the simulation system along the z-direction is then melted by increasing that region's temperature to 2700 K in the NVT ensemble for 50 ps while fixing the rest of the system. Subsequently, the kinetic energy of the liquid phase is scaled to bring the temperature back to 1860 K; the concentration of the liquid is set to the liquidus value of Ti-3.4 at.% Ni alloy, and the whole system is equilibrated for 0.5 ns. This procedure results in CM coexistence which is used as initial configuration for the free solidification simulation.

At a fixed temperature, one can perform free solidification by reducing the liquid composition ($C_{initial}^{L}$) below the liquidus composition followed by $\mathrm{NP_{zz}T}$ ensemble. Previous MD/MC study by Kavousi et al. [48] focused on predicting the onset of complete solute trapping. Thus, the majority of simulations were performed considering larger driving force (larger solidification velocities). While this study aims to accurately calculate the diffusive velocity for the velocity range relevant to AM. For most metallic systems, the diffusive interface velocity is in the order of 1 m/s [35] which is the upper limit for the solidification velocity in AM [69-71]. In order to obtain the solidification velocities up to 1.5 m/s, $C_{initial}^{L}$ is set to 3.3, 2.8, 2.5, and 2.0 at.%. To maintain the interface temperature at the desired value during the solidification, multiple independent thermostats are used along the solidification direction [56].

Attaining accurate predictions of the diffusive velocity requires larger number of datasets for aforementioned velocity range. For each $C^L_{initial}$, the simulations are repeated ten times ($\mathrm{N_{MD}}$=10) and each MD simulation has 2 interfaces that provide 2 sets of data. The simulations are stopped when the distance between the interfaces becomes smaller than 50 Å such that the interaction between them can be neglected. For each time frame, the trajectory files are analyzed to obtain the interface position and concentration profile across the interface. The interface size in y-direction, as presented in Figure 1(b), is small, and periodic boundary conditions are used in all directions; therefore the interface is considered flat without any notable curvatures. This leads to a more accurate concentration profile across the interface. For each time frame in each simulation, first, we define the interface similar to the method explained previously except that smoothing of ψ is performed over a spherical region. Then, depending on the driving force, at least 10 Å into each side of the interface is binned to determine the concentration profile. Overlapping bins are used in this study to increase the accuracy of the results. The width of each bin is equal to the diameter of Ti atoms (2.86 Å) with 0.48 Å spacing between the lower edges of the bins. Using this information, one can obtain the nonequilibrium partition coefficient as a function of solidification velocity [48].

3 Results and Discussion

3.1 Material properties determined by MD simulations

From the MD-calculated phase diagram, the solidus and liquidus compositions at T=1860 K are estimated to be 0.9 and 3.4 at.%, respectively. In addition, $\mathrm{k_e}$, $\mathrm{m_L^e}$, and $\Delta\mathrm{T_0}$ are directly calculated from the phase diagram (data presented in Table 1) and will be directly used in PF simulations.

The CM interface free energy is an anisotropic property and, for a crystal with cubic symmetry, can be represented by the following equation:

$$\gamma = \gamma_0\,[1 + \delta_1\left(\sum_{i=1}^{3} n_i^4 - \frac{3}{5}\right) + \delta_2(3\,\sum_{i=1}^{3} n_i^4 + 66 n_1^2 n_2^2 n_3^2 - 17/7)], \tag{21}$$

where γ_0 is the average interfacial free energy, δ_1 and δ_2 are the anisotropy parameters, and n_i are the components of the unit vector, $\hat{n}$, normal to the interface plane [49].

Figure 2 shows the variation of $\mathrm{k_B T/bW}< |A(k)|^2 >$ versus k^2 for three different crystal-melt interface orientations with the slope of the fitted line equal to the stiffness value for that orientation. $< >$ denotes the in-plane crystallographic orientation of the interface along the x-direction, and {} denotes the orientation characterized by the normal to the crystallographic plane parallel to the interface. The data shows a deviation from a linear behavior for large values of k^2, thus in the fitting process, new points are added till R^2 for the fit falls below 0.95. Fitting the stiffness values to the relationship based on Equation (21), results in γ_0= 185 mJ/m2, δ_1= 0.02 and δ_2= − 0.0002. In application to two-dimensional (2D)-PF simulations, Equation (21) is used in the reduced form given by:

$$\gamma = \gamma_0\,[1 + \delta_\gamma \cos(4\theta)]. \tag{22}$$

θ is the angle between the interface normal and the x-direction, and δ_γ is the interface anisotropy strength whose values are reported in Table 1.

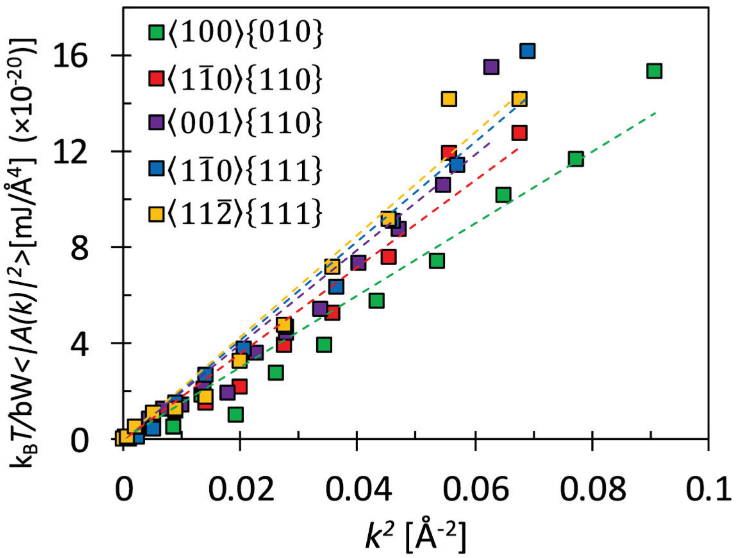

Figure 2. The varition of $\mathrm{k_B T/bW}< |A(k)|^2 >$ versus k^2 for different orientations as obtained from MD simulation. The dashed lines are linear fits with the color of the line matching color of the symbols for the data being fit.

The non-equilibrium partition coefficient can be estimated as $k(V) = c_s/c_L$, where c_s is the average steady-state solute concentration over the solid phase, and c_L is the maximum liquid concentration on the liquid-side of the interface. Figure 3(a) presents the concentration profiles across the interface obtained from MD simulations for three different driving forces. The positive and negative values of distance from the interface reference the melt and crystal sides of the interface, respectively. The concentration profiles are obtained by averaging the concentration profiles over the steady-state portion of the $2N_{MD}$ data sets, and the error bars denote the 95% confidence intervals. Figure 3(a) shows that the concentrations in the liquid phase (right-hand side of the interface) are larger in comparison to the solid phase (left-hand side), with the maximum concentration positioned inside the liquid. For slower solidification, the maximum concentration is obtained inside the liquid phase and far from the CM interface. As the solidification velocity increases, the maximum concentration takes a smaller value and positions closer to the interface. For a slower solidification velocity, the solute atoms have enough time to diffuse ahead of the interface, which results in the partitioning closer to equilibrium, and the resulting concentration gradient is small. With increasing the solidification velocities, both the concentrations in the solid and liquid phases deviate from the solubility limit. The resulting increase/decrease of solute concentration on the solid/liquid-side of the interface leads to increase of non-equilibrium partition coefficient and solute trapping. In addition, concentration profiles in Figure 3(a) suggest that the position of maximum concentration gets closer to the interface when the solidification velocity increases. It is shown in Figure 3(b) that the decrease of distance between the location of maximum concentration on the liquid side, $z_{C_L^{max}}$, and the interface, $z_{interface}$, is a consequence of an increased solidification velocity. The plateau on the concentration profile leads to large uncertainties in identifying the position of maximum concentration. Extending Figure 3(b) to larger velocities would result in smaller scatter in the data, and as noted by Kavousi et al. [48], one would expect to observe an exponential decaying behavior for the change of $z_{C_L^{max}}$ versus the interface velocity. However, due to smaller solidification velocities, Figure 3(b) only presents a descending trend.

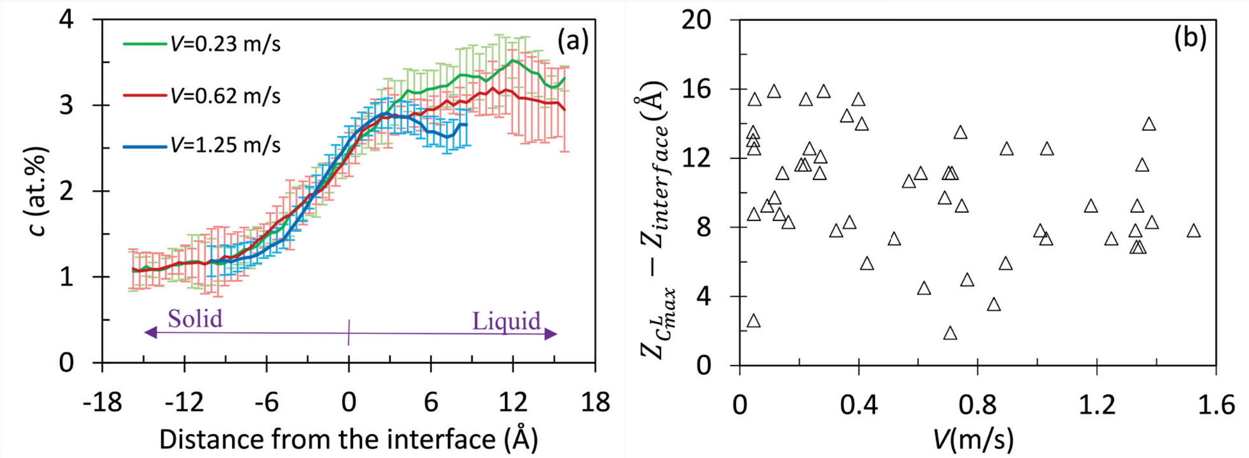

Figure 3. a) Average solute concentration versus the distance from the interface. Positive and negative distances from the interface correspond to the melt (liquid) and crystal (solid) sides of the interface, respectively. Error bars denote the 95% confidence intervals. b) Scatter plot for the distance between the position of maximum concentration and the interface position versus solidification velocity.

Based on the concentration profiles presented in Figure 3(a), the increase in solidification velocity causes changes in the steady-state concentration on the solid-side and the maximum concentration on the liquid-side of the interface. The concentration changes result in an increase in the non-equilibrium partition coefficient, also known as solute trapping, which is also predicted by different analytical models [44, 72] such as the CG model. The partition coefficient from MD simulations can be calculated using:

$$k = \frac{1}{2\mathrm{N}_{\mathrm{MD}}} \sum_{i=1}^{2\mathrm{N}_{\mathrm{MD}}} k_i, \tag{23}$$

where k_i is the average partition coefficient for the i-the interface during the N_{MD} simulations. The resulting nonequilibrium partition coefficients are presented in Figure 4. Ignoring the fluctuations, the partition coefficient profiles calculated from MD simulations are an increasing function of solidification velocity. $\mathrm{V}_{\mathrm{D}}^{\mathrm{CG}}$ is estimated by fitting the velocity-dependent partition coefficient from MD simulations to the CG model [73]. The solid line in Figure 4 is the least-squares fit of MD data to the CG model, and the diffusive interface velocity obtained from the fitting is $\mathrm{V}_{\mathrm{D}}^{\mathrm{CG}}$=1.42 m/s. The diffusive interface velocity will be used later in Equation (7) to obtain the trapping parameter, c_2.

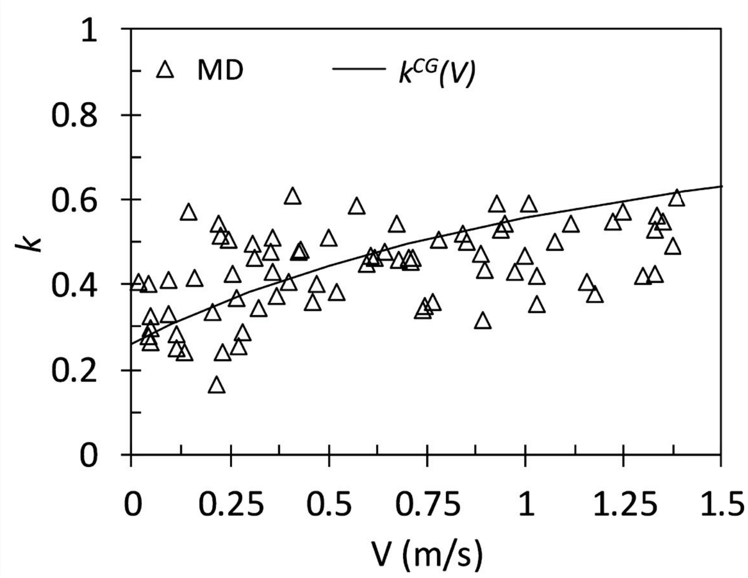

Figure 4. The soldification velocity-dependent partition coefficient from the MD simulations and the corresponding profile of the curve fitted to the CG model to obtain V_D^{CG}.

Table 1 summarizes all the material properties calculated from MD simulations using the MEAM interatomic potential of Ti-Ni. The data obtained from the phase diagram (k_e, m_L^e, ΔT_0) and kinetic coefficient are obtained from our previous works [48, 52] whereas the other properties (D_L, γ_0, δ_γ, Γ, d_0, V_D^{CG}) are calculated in the current study. The PF parameters, $\tau(\vec{n})$ and λ, are obtained based on the thin-interface analysis and using a value for the interface width, W_ϕ. Choosing a small value for W_ϕ provides detailed information on the dendrite morphology, but limits the maximum domain size that can be simulated by the PF model [11]. The increase in solidification velocity decreases the diffusion length, given by the ratio of the liquid diffusivity to the solidification velocity. As solidification velocity increases, the diffusion length becomes so small that the crystallization mechanism transitions from the diffusion-limited to the collision-limited regime [61, 74]. This adds additional constraints on the grid-spacing because obtaining an accurate concentration profile from PF modeling requires having at least 1 grid point across the diffusion length. For investigating the tradeoff between the computational cost and accuracy of PF model predictions, we consider the interface width to be W_ϕ/d_0=1 and 3, and we will further discuss how this affects the PF model predictions. Further discussions on how the number of grid point across the interface width affects the PF simulation results are made in section 3.2.

The PF equations are discretized on a mesh with $0.8\times W_{\phi}$ grid spacing based on the second-order finite difference algorithm. The system of discretized equations is solved numerically using PETSC [75]. Each simulation starts with a thin layer of the solid phase at the bottom of the domain. For the directional solidification, the solid phase grows as the temperature gradient, *G,* translates with the solidification velocity (V) inside the liquid.

Table 1. Material properties for Ti-3.4 at.% Ni: equilibrium partition coefficient, k_e, equilibrium liquidus slope, m_L^e (K/at. %), equilibrium freezing range, ΔT_0 (K), liquid diffusion coefficient, D_L ($\times 10^{-9}$m^2/s), solid-liquid interface free energy, γ_0 (mJ/m^2), and the corresponding anisotropy strength, δ_γ, Gibbs–Thomson coefficient, Γ(K μm), capillary length, d_0 (nm), kinetic coefficient, β (s/(mK)), and diffusive velocity, V_D^{CG}(m/s).

k_e	m_L^e	ΔT_0	D_L	γ_0	δ_γ	Γ	d_0	β	V_D^{CG}
0.26 [a]	25.78 [a]	64.9 [a]	7.92 [b]	185 [b]	0.007 [b]	0.293 [b]	4.90 [b]	0.013 [c]	1.42[b]

[a] Reference [52], [b] This paper, [c] Reference [48].

3.2 Concentration profile: PF simulations versus analytical models

Figure 5 presents the concentration and order parameter profiles versus distance from the interface in both the zero-drag and full-drag limits of our PF model. All the PF simulations are performed under directional solidifications with the thermal gradient of $G=10^7$ K/m and $W_\phi/d_0=1$. The center of diffuse interface is determined to be located at the points where $\phi = 0$, and the solid and liquid phases are to the left- and right-hand side of the interface, respectively. The concentration profiles presented in Figure 5 have some common features characteristic to both modes of the PF model (zero-drag and full-drag). Similar to the MD simulation results presented in Figure 3, the concentration increases from the solid into the liquid with the maximum positioned on the liquid-side of the interface. When the solidification velocity is low, the maximum concentration is located further away from the interface and it gets closer with the increase of solidification velocity.

Another feature obtained from the concentration profiles is the sensitivity of the concentration gradient across the interface, dc/dy, to the solidification velocity. In the PF simulations, solidification is performed under a constant temperature gradient, $G = dT/dy$. To calculate the concentration gradient, the relations for G and $m_L^v = dT/dc$ are combined.

$$\frac{dc}{dy} = \frac{G}{m_L^v}, \tag{24}$$

$$m_L^v = \mathrm{m}_\mathrm{L}^\mathrm{e} f\big(k(V)\big). \tag{25}$$

m_L^v is the kinetic liquidus line slope, and $\mathfrak{D}$ is the drag coefficient. MD studies by Kavousi [48] showed for Ti-3.4 at.%Ni, the drag coefficient is around 0.2, while the PF model, with zero-drag and full-drag modes, considers it to be 0 or 1, respectively. Given by Equation (20), $f\big(k(V)\big)$ takes the value 1 when no-solute trapping is observed, which is equivalent to the equilibrium state. As the solidification velocity increases, $f\big(k(V)\big)$ becomes greater than 1, resulting in an increase in the absolute value of m_L^v. Thus, as the solidification velocity increases, based on Equation (24), the concentration gradient decreases. This justifies the difference in concentration profiles presented in Figure 3.

All parabolic PF models, such as ours, assume the interface to be in local equilibrium. The one-dimensional steady-state solution of the PF equations shows that the interface width calculated by these models do not change with the solidification velocity [76]. Figure 5(b) shows the order parameter shape and width do not change significantly with the solidification velocity. Similarly, MD results [48] showed that the changes in interface width are negligible up to $V = \mathrm{V_D^{CG}}$. As the solidification velocity exceeds $\mathrm{V_D^{CG}}$, the parabolic PF models do not predict the reduction of the interface width with velocity which was observed in MD simulations. Therefore, the hyperbolic PF models [25, 27, 77] are more suitable options for the rapid solidification simulations when the solidification velocity is larger than $\mathrm{V_D^{CG}}$. It should be mentioned that performing quantitative hyperbolic PF simulations is not possible yet.

Despite the qualitative similarities in concentration profiles, the predictions for full-drag and zero-drag modes are not quantitatively similar. There is a clear difference between the solid and liquid concentration values between the two limits, and this difference increases with increasing solidification velocity. A deeper investigation of the concentration on the solid and liquid-side of the interface is needed for a better comparison of the two modes of the PF model.

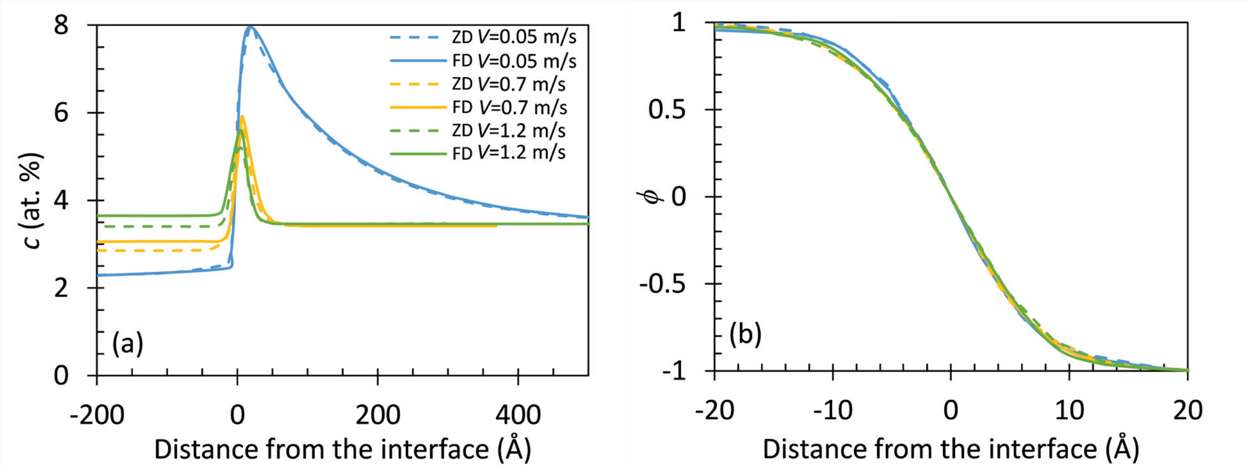

Figure 5. a) Concentration profile, and b) order parameter profile calculated from the PF model with full-drag (FD) and zero drag (ZD) modes under three solidification conditions *V*=0.05, 0.7, and 1.2 m/s

MD-calculated concentration values on the solid and liquid sides of the interface are not quantitatively comparable with PF simulations. As discussed previously, solidification in MD simulations can be performed by either decreasing the concentration of solute in the bulk liquid below the liquidus value while keeping the temperature of the system fixed, or decreasing the temperature of the liquid phase below the value obtained from the phase diagram while keeping the concentration on the liquid side of the interface fixed. The second method requires having full control over the concentration profile close to the interface on the liquid side. Concentration profile, as showed in Figure 3, is a dynamic property, and therefore performing solidification with this method is not possible. In the first method, the temperature is the property that should be fully controlled, and the concentration profile is the property obtained during the solidification. Multiple local thermostats enable us to use this method in MD simulations. On the other hand, in PF simulations, the alloy composition is kept constant and the solidification is performed by applying a constant temperature gradient. We will compare the concentration values on the liquid and solid side of the interface from the PF simulations with those from analytical models.

Based on the analysis of the diffusion field around the dendrite tip by Kurz-Fisher [78], the solid concentration, c_S, and radius of the dendrite tip, R, are related to the solidification condition and material properties [79]:

$$G_c = \frac{V}{\mathrm{D_L}} \mathrm{k_e} c_s (1 - \mathrm{k_e}), \tag{26}$$

$$R = 2\pi \left[\frac{\Gamma}{\mathrm{m_L^e} G_c - G}\right]^{\frac{1}{2}}, \tag{27}$$

$$c_s = \frac{\mathrm{k_e c_0}}{1 - (1 - \mathrm{k_e}) Iv(P)}, \tag{28}$$

$$Iv(P) \equiv \sqrt{\pi P} \exp(P)\, erfc\left(\sqrt{P}\right), \tag{29}$$

$$P = \frac{VR}{2\mathrm{D_L}}, \tag{30}$$

$$c_L = \frac{c_S}{k(V)} = \frac{\mathrm{k_e} c_0}{k(V)(1 - (1 - \mathrm{k_e}) Iv(P))}. \tag{31}$$

G_c is the composition gradient in the liquid, P is the Peclet number, and Ivantsov function, $Iv(P)$, represent the solution of solute diffusion problem for the steady-state growth of dendrite with parabolic tip. The liquid composition can be calculated based on the analytical solid concentrations and the CG model, given by Equation (31). Figure 6 compares the solid and liquid concentrations from the analytical model and PF simulations. The data is obtained using $W_\phi/\mathrm{d_0}$= 1 and 3 to investigate the dependency of this PF model on the interface width. All the PF simulations are performed under directional solidifications with the thermal gradient of G=10^7 K/m. The liquid composition, c_L, is calculated based on the c_s and non-equilibrium partition coefficient from the CG model, presented by Equation (16). For the case where the interface width is equal to the capillary length, both c_s and c_L are in general underestimated for smaller solidification velocities. As the solidification velocity increases, the PF and analytical results get closer. Both concentrations are slightly overestimated when the solidification velocity gets close to $\mathrm{V_D^{CG}}$. Also, when V<0.9 m/s, there is a slight difference between the predictions of full-drag and zero-drag modes of the PF model. This difference amplifies as the interface width is increased. When V>0.4 m/s, the liquid concentration in the full-drag limit of PF model presents a sudden increase with the increase in the solidification velocity, which can lead to the underestimations of solute trapping. For the zero-drag limit, the increase in c_L is not significant unless the solidification velocity exceeds 0.7 m/s. For $W_\phi/\mathrm{d_0}$=3, the grid spacing used in the numerical solution is 11.76 nm, which is larger than the diffusion length corresponding to V=0.7 m/s (11.3 nm). We performed the convergence study on how the number of points across diffusion length affects the partition coefficient for V=0.7 m/s. The results suggest that the PF modeling results in accurate predictions if at least two grid points are placed across the diffusion length. This also explains the deviation of the PF results from the analytical models for higher solidification velocities. Also it should be noted that our model will retain its accurate predictions even using a larger interface width for solidification velocities smaller than 0.7 m/s.

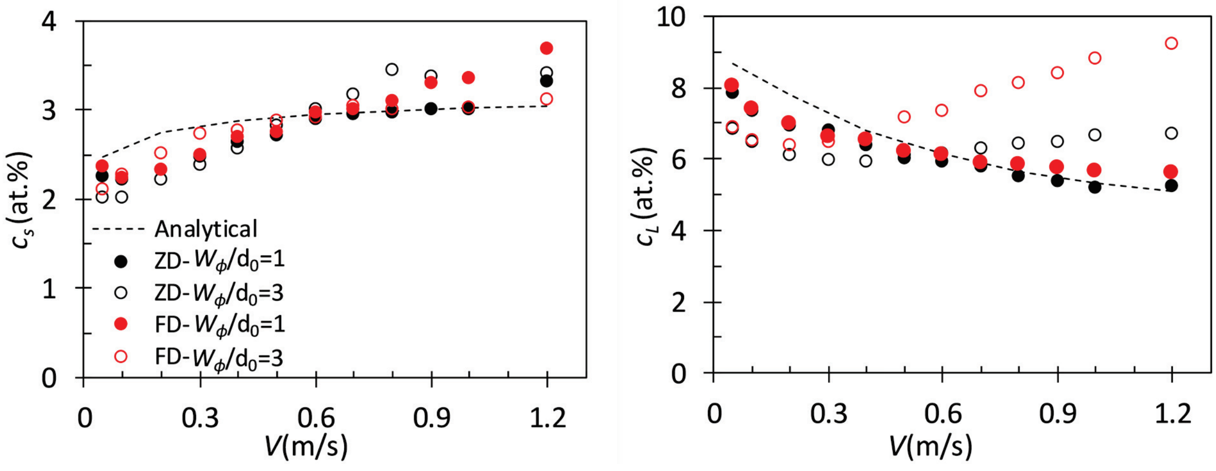

Figure 6. Solid (c_S) and liquid (c_L) concentrations at the interface from the Kurz-Fisher analytical model [78] and PF simulations for both zero-drag (ZD) and full-drag (FD) modes. The PF simulations are performed considering two different interface widths: W_ϕ/d$_0$=1 and 3.

3.3 Solute trapping: PF versus MD simulations

Performing the simulations with the PP model needs prior knowledge of the characteristic solute trapping velocity, $\mathrm{V_D^{PF}}$, to calculate the trapping parameter. Using thin interface analysis, Pinomaa and Provatas [31] showed that the non-equilibrium partition coefficient predicted by their model follows Equation (32). Therefore, $\mathrm{V_D^{PF}}$ is defined such that the difference between the partition coefficient obtained using Equation (32) and the CG model is minimized. The solute trapping velocity is later used to parameterize the trapping coefficient (c_2') in the anti-trapping flux (a_t'). For the material of interest, $\mathrm{V_D^{PF}}$=0.975 m/s.

$$k^{PF}(V) = \mathrm{k_e}\exp\left(\sqrt{2}\left(1-k^{PF}(V)\right)\frac{V}{\mathrm{V_D^{PF}}}\right), \tag{32}$$

$$\mathrm{c}_2' = \frac{\mathrm{D_L}}{\mathrm{V_D^{CG}}W_\phi} \quad , \tag{33}$$

$$a_t'(\phi) = \frac{1}{2\sqrt{2}}\left(1-\mathrm{c}_2'\left(1-\phi^2\right)\right). \tag{34}$$

The PF simulations using both the current and the PP models are performed with the thermal gradient of $G=10^7$ K/m and different ratios of W_ϕ/d_0 (1 and 3) to investigate the dependency of both PF models on the interface width.

Figure 7 compares the partition coefficient calculated by our PF model, the analytical CG model, and the PP model. For the simulations with the interface width equal to the capillary length, our PF model for both the zero-drag and full-drag limit show excellent agreement with the CG model for velocities close to V_D^{CG}. The PP model with full-drag presents a similar performance with only a sudden drop in the partition coefficient for $V>1.0$ m/s. However, the PP model with zero-drag does not predict any solute trapping. The reason is hidden in the formulation of the PP model. Based on the material properties, given in Table 1, some coefficients defined in thin interface analysis of the PP model will take negative values which result in failure of the model in predicting the solute trapping. To solve this problem, the interface width should be considered much smaller than the capillary length, which contradicts the purpose of using the diffuse interface approach.

The PF model parameterization of the PP model is performed by fitting the experimental non-equilibrium partition coefficient to the "expected" mathematical equation from the PF model. In order to develop a fully predictive computational framework for rapid solidification, in this work, the PF parametrization is performed by fitting the MD simulations to the CG model. The diffusive interface velocity obtained from the fitting is used in estimating the trapping coefficient. Our previous work on Si-9at.%As showed the full-drag limit of the present PF model presents accurate solute trapping predictions [32]. While in this work on Ti-3.4at.% Ni, we showed that the zero drag mode provided better results. The difference in the solute and solvent atom size, viscosity, and temperature of the liquid phase can affect the amount of free energy dissipated due to the solute redistribution. Therefore, different binary systems can have different drag coefficients. Consequently, our proposed computational framework with estimations of the drag coefficient based on the method proposed in [48], leads to more accurate solute trapping estimations.

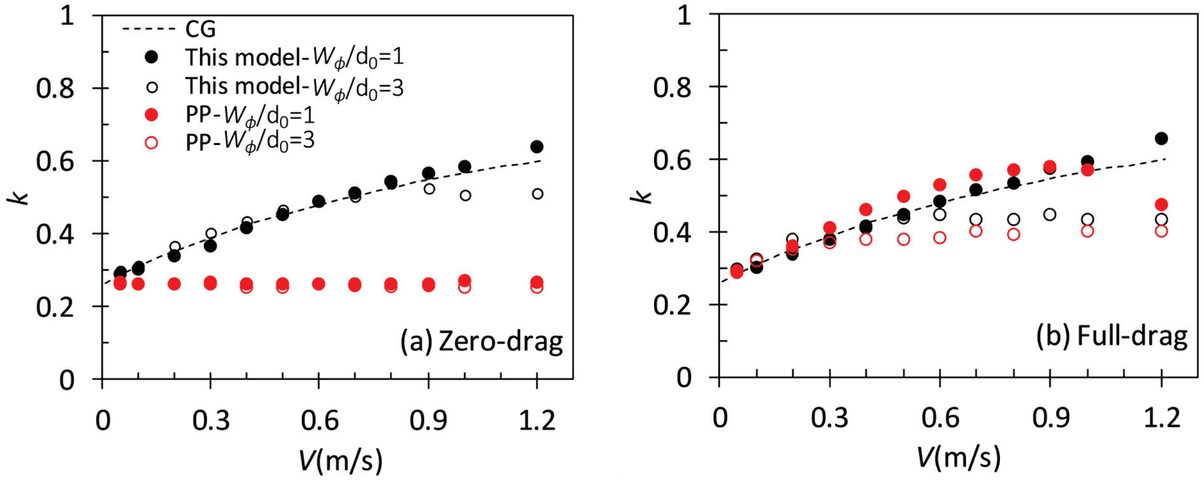

Figure 7. The non-equilibrium partition coefficient from the CG model compared with the current PF model and the PP model using zero-drag and full-drag modes. The PF simulations are performed considering two different interface widths: W_ϕ/d_0=1 and 3.

3.4 Three-dimensional PF simulation of directional solidification

We also created the three-dimensional (3D) version of the model to investigate any discrepancies between 2D and 3D simulations. 2D and 3D PF simulations of directional solidification are performed with zero drag considering $G=10^7$ K/m. Figure 8 shows the concentrations across the CM interface as a function of solidification velocity obtained by PF simulations and analytical models [78]. The concentrations on the solid- and liquid-side of the interface from both the 2D and 3D-PF simulations with $W_\phi=d_0$, as presented in Figure 8, are in good agreement with the analytical results [78], with 3D-PF simulations resulting in slightly more accurate predictions. While considering $W_\phi=3\times d_0$, the accuracy of the 3D-PF simulations slightly drops with the increase of solidification velocity. The results show that 2D simulations can provide reasonable predictions in rapid solidification as simple microstructures are expected due to cellular growth.

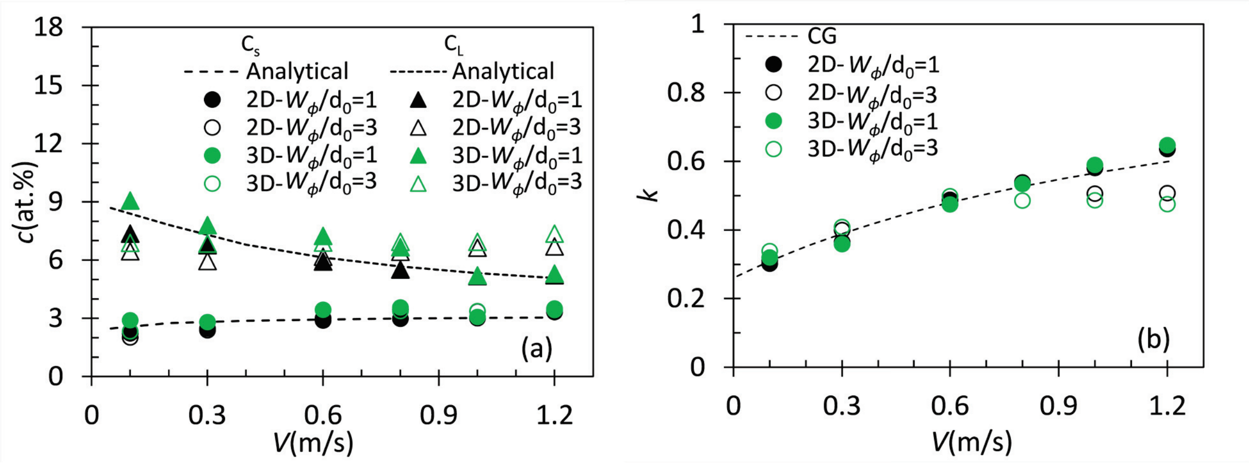

Figure 8. (a) Solid (c_S) and liquid (c_L) concentrations at the interface from the Kurz-Fisher analytical model [78] compared with 2D and 3D-PF simulations of the current PF model. (b) The non-equilibrium partition coefficient from the CG model compared with the 2D and 3D-PF simulations of the current model. The PF simulations are performed considering two different interface widths: W_ϕ/d$_0$=1 and 3.

3.5 Primary dendritic arm spacing: PF simulations versus analytical models

Microsegregation and PDAS are two important factors that affect the mechanical properties of materials [80-83]. The previous study by Kavousi and Asle Zaeem [32] raised the question regarding the reliability of the PF-calculated PDAS when the model lacks accurate solute trapping predictions. To answer this equation, a more detailed investigation of microstructure evolution is performed here by comparing the results of PF simulations with the analytical models. Burden-Hunt (BH) [84] is a theoretical model, given by Equation (35), which relates PDAS to the geometry of cells, material properties, and processing parameters:

$$PDAS = 2.83(\mathrm{k_e}\Gamma\Delta\mathrm{T_0}\mathrm{D_L})^{0.25}G^{-0.5}V^{-0.25}. \qquad (35)$$

Figure 9 compares the PDAS predictions of the current PF simulations with the analytical HB model, considering W_ϕ/d$_0$=1 and 3. The PF simulations are performed under directional solidification with two thermal gradients of G=10^7 and 1.5×10^7 K/m. In general, the results of zero-drag limit for both interface widths are close to each other and present a nearly linear relation with $G^{-0.5}V^{-0.25}$, while the results of the full-drag limit scatter. Analyzing the results of PF simulations reveals that the PDAS predictions are influenced mainly by partitioning. The results of the zero-drag limit of the PF model are not largely affected by the interface width unless the cooling rate ($G \times V$) reaches 1.2×10^7 K/s. The considerably large deviation in the PDAS predictions does not occur unless the solid and liquid concentrations and the resulting partition coefficient deviate from the analytical models, as presented in Figures 6 and 7. For the full-drag mode, the deviation between the PDAS predictions for the two interface widths is observed at a smaller cooling rate (0.45×10^7 K/s). There are experimental [85] and PF [32, 86, 87] studies in the literature that have also reported deviations of PDAS from the results of analytical models, especially during rapid solidification. The difference was always attributed to the rapid solidification conditions. We have observed similar behavior in this paper, where the PF results do not match quantitatively with the analytical BH model. On the other hand, we have shown that when the PF model fails to predict solute trapping accurately, the PDAS results scatter and are not reliable. Therefore, the inconsistency between the PDAS results in literature should not be only attributed to the physics of rapid solidification. The results presented in this work suggest that the inconsistency of the PF results in the literature can be related to the failure of PF models in predicting solute trapping. Thus, having a PF model with an accurate solute trapping prediction is critical before performing the PF simulations for microstructure evolution studies.

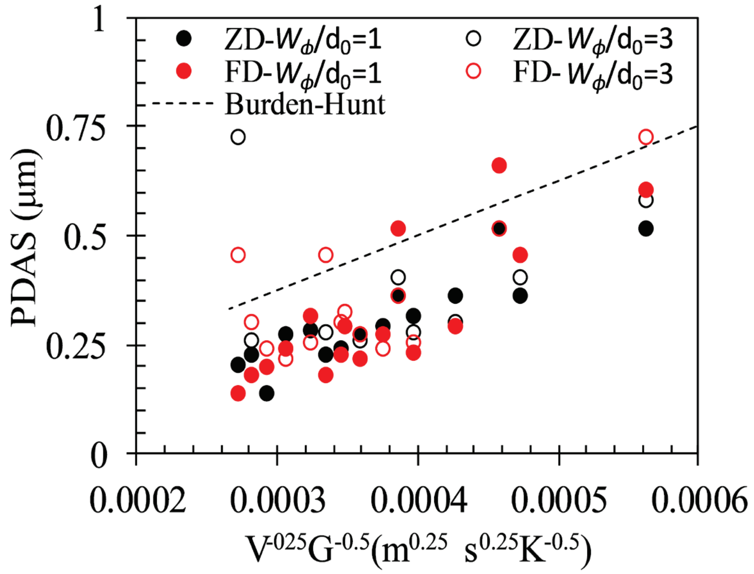

Figure 9. Comparison of PDAS calculated by the theoretical model of Burden Hunt [84] with the current PF model under zero-drag (ZD) and full-drag (FD) modes with W_ϕ/d_0=1 and 3.

4 Conclusion

We have presented a quantitative computational framework by integrating atomistic simulations and PF modeling for investigating the solute trapping and cellular growth during rapid solidification. The accuracy of this model is tested for rapid solidification of Ti-3.4at.%Ni alloy. Our computational framework is the first that can predict the partitioning and microstructural evolution during solidification of alloys, at solidification velocities relevant to additive manufacturing without any fitting to experiments. We showed that MD simulations could determine all the material properties required to parametrize the PF model of rapid solidification; these material properties include anisotropic crystal-melt interface free energy, kinetic coefficient, drag coefficient, and the diffusive velocity. Compared to the analytical models and MD simulation results, the proposed atomistic-informed PF model accurately predicts the solute trapping and dendritic arm spacing. One of the main advantages of our PF model over the existing models is that the accuracy of the results is not noticeably affected by the interface width unless the solidification velocity is close to the diffusive velocity. Consequently, one can argue that the interface width dependence observed in the existing PF models can be the source of inconsistencies in the relationships between the PDAS and solidification conditions reported in many previous studies.

Acknowledgment

This study was supported by the National Science Foundation, NSF-CMMI 2031800 and NSF-OIA 1541079, and by NASA 80NSSC19K0569. SK and MAZ are grateful for supercomputing time allocation provided by the Extreme Science and Engineering Discovery Environment (XSEDE), award number TG-DMR140008.

CRediT Author Statement

Sepideh Kavousi: Conceptualization, Methodology, Software, Formal analysis, Writing- Original draft preparation. **Brian Novak:** Conceptualization, Methodology, Software, Formal analysis, Writing- Reviewing and Editing. **Dorel Moldovan:** Conceptualization, Methodology, Writing- Reviewing and Editing. **Mohsen Asle Zaeem:** Supervision, Conceptualization, Methodology, Formal analysis, Writing- Reviewing and Editing, Funding Acquisition.

Data availability

All necessary data generated or analyzed during this study are included in this published article, and other auxiliary data are available from the corresponding author on reasonable request.

Declaration of Competing Interest

The authors declare no competing interests.

References

[1] W.E. Frazier, Metal Additive Manufacturing: A Review, Journal of Materials Engineering and Performance 23(6) (2014) 1917-1928.
[2] NIST, Measurement Science Roadmap for Metal-Based Additive Manufacturing, US Department of Commerce, National Institute of Standards and Technology, Prepared by Energetics Incorporated (May 2013).
[3] D.L. Bourell, D.W. Rosen, M.C. Leu, The roadmap for additive manufacturing and its impact, 3D Printing and Additive Manufacturing 1(1) (2014) 6-9.
[4] S. Pauly, P. Wang, U. Kühn, K. Kosiba, Experimental determination of cooling rates in selectively laser-melted eutectic Al-33Cu, Additive Manufacturing 22 (2018) 753-757.
[5] M. Ma, Z. Wang, X. Zeng, A comparison on metallurgical behaviors of 316L stainless steel by selective laser melting and laser cladding deposition, Materials Science and Engineering: A 685 (2017) 265-273.
[6] X. Wang, L.N. Carter, B. Pang, M.M. Attallah, M.H. Loretto, Microstructure and yield strength of SLM-fabricated CM247LC Ni-Superalloy, Acta Materialia 128 (2017) 87-95.
[7] B. Zheng, Y. Zhou, J. Smugeresky, J. Schoenung, E. Lavernia, Thermal behavior and microstructure evolution during laser deposition with laser-engineered net shaping: part II. Experimental investigation and discussion, Metallurgical and materials transactions A 39(9) (2008) 2237-2245.
[8] Z. Tarzimoghadam, S. Sandlöbes, K.G. Pradeep, D. Raabe, Microstructure design and mechanical properties in a near-α Ti–4Mo alloy, Acta Materialia 97 (2015) 291-304.
[9] H. Rao, S. Giet, K. Yang, X. Wu, C.H.J. Davies, The influence of processing parameters on aluminium alloy A357 manufactured by Selective Laser Melting, Materials & Design 109 (2016) 334-346.
[10] Z.C. Luo, H.P. Wang, Primary dendrite growth kinetics and rapid solidification mechanism of highly undercooled Ti-Al alloys, Journal of Materials Science & Technology 40 (2020) 47-53.
[11] C. Körner, M. Markl, J.A. Koepf, Modeling and Simulation of Microstructure Evolution for Additive Manufacturing of Metals: A Critical Review, Metallurgical and Materials Transactions A 51(10) (2020) 4970-4983.
[12] Y. Kok, X.P. Tan, P. Wang, M.L.S. Nai, N.H. Loh, E. Liu, S.B. Tor, Anisotropy and heterogeneity of microstructure and mechanical properties in metal additive manufacturing: A critical review, Materials & Design 139 (2018) 565-586.

[13] N. Gupta, C. Weber, S. Newsome, Additive manufacturing: status and opportunities, Science and Technology Policy Institute, Washington (2012).

[14] B. Echebarria, R. Folch, A. Karma, M. Plapp, Quantitative phase-field model of alloy solidification, Physical Review E 70(6) (2004) 061604.

[15] A. Karma, Phase-field formulation for quantitative modeling of alloy solidification, Physical Review Letters 87(11) (2001) 115701.

[16] W. J. Boettinger, J. A. Warren, C. Beckermann, A. Karma, Phase-Field Simulation of Solidification, Annual Review of Materials Research 32(1) (2002) 163-194.

[17] M.A. Harrison, 4/67–1R Theory of Self-Reproducing Automata. 1966. John von Neumann. Arthur W. Burks, Editor. University of Illinois Press, American Documentation 18(4) (1967) 254-254.

[18] M. Asle Zaeem, H. Yin, S.D. Felicelli, Modeling dendritic solidification of Al–3%Cu using cellular automaton and phase-field methods, Applied Mathematical Modelling 37(5) (2013) 3495-3503.

[19] M. Rappaz, C.A. Gandin, Probabilistic modelling of microstructure formation in solidification processes, Acta Metallurgica et Materialia 41(2) (1993) 345-360.

[20] H.L. Wei, G.L. Knapp, T. Mukherjee, T. DebRoy, Three-dimensional grain growth during multi-layer printing of a nickel-based alloy Inconel 718, Additive Manufacturing 25 (2019) 448-459.

[21] H.L. Wei, J.W. Elmer, T. DebRoy, Three-dimensional modeling of grain structure evolution during welding of an aluminum alloy, Acta Materialia 126 (2017) 413-425.

[22] D. Tourret, A. Karma, Multiscale dendritic needle network model of alloy solidification, Acta Materialia 61(17) (2013) 6474-6491.

[23] D. Tourret, A. Karma, Multi-scale needle-network model of complex dendritic microstructure formation, Iop Conference Series: Materials Science and Engineering 33 (2012).

[24] N. Ahmad, A. Wheeler, W.J. Boettinger, G.B. McFadden, Solute trapping and solute drag in a phase-field model of rapid solidification, Physical Review E 58(3) (1998) 3436.

[25] P.K. Galenko, E.V. Abramova, D. Jou, D.A. Danilov, V.G. Lebedev, D.M. Herlach, Solute trapping in rapid solidification of a binary dilute system: A phase-field study, Physical Review E 84(4) (2011) 041143.

[26] T. Keller, G. Lindwall, S. Ghosh, L. Ma, B.M. Lane, F. Zhang, U.R. Kattner, E.A. Lass, J.C. Heigel, Y. Idell, M.E. Williams, A.J. Allen, J.E. Guyer, L.E. Levine, Application of finite element, phase-field, and CALPHAD-based methods to additive manufacturing of Ni-based superalloys, Acta Materialia 139 (2017) 244-253.

[27] L. Zhang, E.V. Danilova, I. Steinbach, D. Medvedev, P.K. Galenko, Diffuse-interface modeling of solute trapping in rapid solidification: Predictions of the hyperbolic phase-field model and parabolic model with finite interface dissipation, Acta Materialia 61(11) (2013) 4155-4168.

[28] N. Provatas, K. Elder, Phase-field methods in materials science and engineering, John Wiley & Sons2011.

[29] T. Pinomaa, J.M. McKeown, J.M.K. Wiezorek, N. Provatas, A. Laukkanen, T. Suhonen, Phase field modeling of rapid resolidification of Al-Cu thin films, Journal of Crystal Growth 532 (2020) 125418.

[30] S. Ghosh, L. Ma, N. Ofori-Opoku, J.E. Guyer, On the primary spacing and microsegregation of cellular dendrites in laser deposited Ni–Nb alloys, Modelling and simulation in materials science and engineering 25(6) (2017) 065002.

[31] T. Pinomaa, N. Provatas, Quantitative phase field modeling of solute trapping and continuous growth kinetics in quasi-rapid solidification, Acta Materialia 168 (2019) 167-177.
[32] S. Kavousi, M. Asle Zaeem, Quantitative Phase-Field Modeling of Solute Trapping in Rapid Solidification, Acta Materialia submitted (2020).
[33] T. Pinomaa, M. Lindroos, M. Walbrühl, N. Provatas, A. Laukkanen, The significance of spatial length scales and solute segregation in strengthening rapid solidification microstructures of 316L stainless steel, Acta Materialia 184 (2020) 1-16.
[34] R. Reitano, P.M. Smith, M.J. Aziz, Solute trapping of group III, IV, and V elements in silicon by an aperiodic stepwise growth mechanism, Journal of Applied Physics 76(3) (1994) 1518-1529.
[35] J. Kittl, P. Sanders, M. Aziz, D. Brunco, M. Thompson, Complete experimental test of kinetic models for rapid alloy solidification, Acta Materialia 48(20) (2000) 4797-4811.
[36] K. Keşlioğlu, N. Maraşlı, Solid–liquid interfacial energy of the eutectoid β phase in the Al–Zn eutectic system, Materials Science and Engineering: A 369(1) (2004) 294-301.
[37] K. Keşlıoğlu, M. Gündüz, H. Kaya, E. Çadırlı, Solid–liquid interfacial energy in the Al–Ti system, Materials Letters 58(24) (2004) 3067-3073.
[38] N. Maraşli, J.D. Hunt, Solid-liquid surface energies in the Al□CuAl2, Al□NiAl3 and Al□Ti systems, Acta Materialia 44(3) (1996) 1085-1096.
[39] D. Turnbull, Formation of Crystal Nuclei in Liquid Metals, Journal of Applied Physics 21(10) (1950) 1022-1028.
[40] R.E. Napolitano, S. Liu, Three-dimensional crystal-melt Wulff-shape and interfacial stiffness in the Al-Sn binary system, Physical Review B 70(21) (2004) 214103.
[41] S. Walder, P.L. Ryder, A simple technique for the measurement of dendritic growth rates in undercooled metallic melts and its application to Ni and Ti, Materials Science and Engineering: A 203(1) (1995) 197-202.
[42] P. R. Algoso, A. S. Altgilbers, W. Hofmeister, R. J. Bayuzick, The Solidification Velocity of Undercooled Nickel and Titanium Alloys with Dilute Solute, 2003.
[43] M. Aziz, J. Tsao, M.O. Thompson, P. Peercy, C. White, Solute trapping: comparison of theory with experiment, Physical Review Letters 56(23) (1986) 2489.
[44] M.J. Aziz, T. Kaplan, Continuous growth model for interface motion during alloy solidification, Acta Metallurgica 36(8) (1988) 2335-2347.
[45] J.A. Kittl, P.G. Sanders, M.J. Aziz, D.P. Brunco, M.O. Thompson, Complete experimental test of kinetic models for rapid alloy solidification, Acta Materialia 48(20) (2000) 4797-4811.
[46] Y. Yang, H. Humadi, D. Buta, B.B. Laird, D. Sun, J.J. Hoyt, M. Asta, Atomistic simulations of nonequilibrium crystal-growth kinetics from alloy melts, Physical review letters 107(2) (2011) 025505.
[47] S. Raman, J.J. Hoyt, P. Saidi, M. Asta, Molecular dynamics study of the thermodynamic and kinetic properties of the solid-liquid interface in FeMn, Computational Materials Science 182 (2020) 109773.
[48] S. Kavousi, B.R. Novak, J. Hoyt, D. Moldovan, Interface kinetics of rapid solidification of binary alloys by atomistic simulations: Application to Ti-Ni alloys, Computational Materials Science 184 (2020) 109854.
[49] J.J. Hoyt, M. Asta, Atomistic computation of liquid diffusivity, solid-liquid interfacial free energy, and kinetic coefficient in Au and Ag, Physical Review B 65(21) (2002) 214106.
[50] E. Asadi, M. Asle Zaeem, S. Nouranian, M.I. Baskes, Quantitative modeling of the equilibration of two-phase solid-liquid Fe by atomistic simulations on diffusive time scales, Physical Review B 91(2) (2015) 024105.

[51] S. Kavousi, B.R. Novak, M. Asle Zaeem, D. Moldovan, Combined molecular dynamics and phase field simulation investigations of crystal-melt interfacial properties and dendritic solidification of highly undercooled titanium, Computational Materials Science 163 (2019) 218-229.
[52] S. Kavousi, B.R. Novak, M.I. Baskes, M. Asle Zaeem, D. Moldovan, Modified embedded-atom method potential for high-temperature crystal-melt properties of Ti–Ni alloys and its application to phase field simulation of solidification, Modelling and Simulation in Materials Science and Engineering 28(1) (2019) 015006.
[53] J.J. Hoyt, S. Raman, N. Ma, M. Asta, Unusual temperature dependence of the solid-liquid interfacial free energy in the Cu-Zr system, Computational Materials Science 154 (2018) 303-308.
[54] T. Frolov, Y. Mishin, Solid-liquid interface free energy in binary systems: Theory and atomistic calculations for the (110) Cu–Ag interface, The Journal of Chemical Physics 131(5) (2009) 054702.
[55] A.A. Potter, J.J. Hoyt, A molecular dynamics simulation study of the crystal–melt interfacial free energy and its anisotropy in the Cu–Ag–Au ternary system, Journal of Crystal Growth 327(1) (2011) 227-232.
[56] J. Monk, Y. Yang, M.I. Mendelev, M. Asta, J.J. Hoyt, D.Y. Sun, Determination of the crystal-melt interface kinetic coefficient from molecular dynamics simulations, Modelling and Simulation in Materials Science and Engineering 18(1) (2010) 015004.
[57] J.J. Hoyt, B. Sadigh, M. Asta, S.M. Foiles, Kinetic phase field parameters for the Cu–Ni system derived from atomistic computations, Acta Materialia 47(11) (1999) 3181-3187.
[58] Y. Oshida, 2 - Materials Classification, in: Y. Oshida (Ed.), Bioscience and Bioengineering of Titanium Materials (Second Edition), Elsevier, Oxford, 2013, pp. 9-34.
[59] P.A. Kobryn, S. Semiatin, The laser additive manufacture of Ti6Al4V, Jom 53 (2001) 40-42.
[60] J.W. Barrett, H. Garcke, R. Nürnberg, Phase Field Models Versus Parametric Front Tracking Methods: Are They Accurate and Computationally Efficient?, Communications in Computational Physics 15(2) (2014) 506-555.
[61] M.J. Aziz, W.J. Boettinger, On the transition from short-range diffusion-limited to collision-limited growth in alloy solidification, Acta Metallurgica et Materialia 42(2) (1994) 527-537.
[62] M.J. Aziz, J.Y. Tsao, M.O. Thompson, P.S. Peercy, C.W. White, Solute Trapping: Comparison of Theory with Experiment, Physical Review Letters 56(23) (1986) 2489-2492.
[63] S. Plimpton, Fast Parallel Algorithms for Short-Range Molecular Dynamics, Journal of Computational Physics 117(1) (1995) 1-19.
[64] R.T. McGibbon, K.A. Beauchamp, M.P. Harrigan, C. Klein, J.M. Swails, C.X. Hernández, C.R. Schwantes, L.-P. Wang, T.J. Lane, V.S. Pande, MDTraj: A Modern Open Library for the Analysis of Molecular Dynamics Trajectories, Biophys J 109(8) (2015) 1528-1532.
[65] M. Newville, T. Stensitzki, D. B. Allen, A. Ingargiola, LMFIT: Non-Linear Least-Square Minimization and Curve-Fitting for Python¶, 2014.
[66] A. Stukowski, Visualization and analysis of atomistic simulation data with OVITO–the Open Visualization Tool, Modelling and Simulation in Materials Science and Engineering 18(1) (2009) 015012.
[67] J. Hoyt, M. Asta, A. Karma, Atomistic and continuum modeling of dendritic solidification, Materials Science & Engineering R-reports 41 (2003) 121-163.
[68] D.Y. Sun, M. Asta, J.J. Hoyt, Kinetic coefficient of Ni solid-liquid interfaces from molecular-dynamics simulations, Physical Review B 69(2) (2004) 024108.

[69] C. Pei, D. Shi, H. Yuan, H. Li, Assessment of mechanical properties and fatigue performance of a selective laser melted nickel-base superalloy Inconel 718, Materials Science and Engineering: A 759 (2019) 278-287.

[70] Y. Luo, B. Zhang, C. Li, G. Chen, G.P. Zhang, Detecting void-induced scatter of fatigue life of selective laser melting-fabricated Inconel 718 using miniature specimens, Materials Research Express 6 (2019).

[71] H.Y. Wan, Z.J. Zhou, C.P. Li, G.F. Chen, G.P. Zhang, Effect of scanning strategy on mechanical properties of selective laser melted Inconel 718, Materials Science and Engineering: A 753 (2019) 42-48.

[72] P. Galenko, S. Sobolev, Local nonequilibrium effect on undercooling in rapid solidification of alloys, Physical Review E 55(1) (1997) 343-352.

[73] S.J. Cook, P. Clancy, Impurity segregation in Lennard-Jones A/AB heterostructures. I. The effect of lattice strain, The Journal of Chemical Physics 99(3) (1993) 2175-2191.

[74] P.K. Galenko, V. Ankudinov, K. Reuther, M. Rettenmayr, A. Salhoumi, E.V. Kharanzhevskiy, Thermodynamics of rapid solidification and crystal growth kinetics in glass-forming alloys, Philos Trans A Math Phys Eng Sci 377(2143) (2019) 20180205-20180205.

[75] S. Balay, S. Abhyankar, M. Adams, J. Brown, P. Brune, K. Buschelman, L. Dalcin, V. Eijkhout, W. Gropp, D. Kaushik, Petsc users manual revision 3.8, Argonne National Lab.(ANL), Argonne, IL (United States), 2017.

[76] A. Salhoumi, P.K. Galenko, Analysis of interface kinetics: solutions of the Gibbs-Thomson-type equation and of the kinetic rate theory, IOP Conference Series: Materials Science and Engineering 192 (2017) 012014.

[77] V. Lebedev, E. Abramova, D. Danilov, P. Galenko, Phase-field modeling of solute trapping: Comparative analysis of parabolic and hyperbolic models, International Journal of Materials Research (formerly Zeitschrift fuer Metallkunde) 101 (2010) 473-479.

[78] W. Kurz, D.J. Fisher, Fundamentals of solidification.

[79] W. Kurz, B. Giovanola, R. Trivedi, Theory of microstructural development during rapid solidification, Acta Metallurgica 34(5) (1986) 823-830.

[80] Y.-J. Liang, A. Li, X. Cheng, X.-T. Pang, H.-M. Wang, Prediction of primary dendritic arm spacing during laser rapid directional solidification of single-crystal nickel-base superalloys, Journal of Alloys and Compounds 688 (2016) 133-142.

[81] M.M. Jabbari Behnam, P. Davami, N. Varahram, Effect of cooling rate on microstructure and mechanical properties of gray cast iron, Materials Science and Engineering: A 528(2) (2010) 583-588.

[82] J. Li, H.M. Wang, Microstructure and mechanical properties of rapid directionally solidified Ni-base superalloy Rene′41 by laser melting deposition manufacturing, Materials Science and Engineering: A 527(18) (2010) 4823-4829.

[83] G. Santos, P.R. Goulart, A.A. Couto, A. Garcia, Primary dendrite arm spacing effects upon mechanical properties of an Al–3wt% cu–1wt% li alloy, Properties and Characterization of Modern Materials, Springer2017, pp. 215-229.

[84] M.H. Burden, J.D. Hunt, Cellular and dendritic growth. II, Journal of Crystal Growth 22(2) (1974) 109-116.

[85] M. Tang, P.C. Pistorius, S. Narra, J.L. Beuth, Rapid Solidification: Selective Laser Melting of AlSi10Mg, JOM 68(3) (2016) 960-966.

[86] L. Wu, J. Zhang, Phase Field Simulation of Dendritic Solidification of Ti-6Al-4V During Additive Manufacturing Process, JOM 70(10) (2018) 2392-2399.

[87] S. Sahoo, K. Chou, Phase-field simulation of microstructure evolution of Ti–6Al–4V in electron beam additive manufacturing process, Additive Manufacturing 9 (2016) 14-24.